nature nanotechnology

Article

https://doi.org/10.1038/s41565-023-01576-z

High-density transparent graphene arrays for predicting cellular calcium activity at depth from surface potential recordings

In the format provided by the authors and unedited

High-density Transparent Graphene Arrays for Predicting Cellular Calcium Activity at Depth from Surface Potential Recordings

Mehrdad Ramezani, Jeong-Hoon Kim, Xin Liu, Chi Ren, Abdullah Alothman, Chawina De-Eknamkul, Madison N. Wilson, Ertugrul Cubukcu, Vikash Gilja, Takaki Komiyama, and Duygu Kuzum

Supplementary Discussion

Supplementary Discussion 1

Several constraints limit the use of different materials as multimodal chronic interfaces (Extended Data Table 1). The brittle nature of ITO, for instance, makes it susceptible to crack formation and mechanical degradation [1, 2]. CNTs and nanowires have shown cytotoxicity in many studies raising concerns on biocompatibility [3, 4]. Metal nanowires and meshes might still absorb light leading to light induced artifacts in electrical recordings due to photovoltaic and photothermal effects [5, 6]. PEDOT:PSS might exhibit chronic reliability issues due to delamination [7]. Graphene, however, does not have any of these issues and offers characteristics desirable for multimodal neural. Extended Data Table 1 provides a comparison of electrode area, channel count, electrode pitch, normalized impedance, areal coverage, optical transmittance, and chronic recording reliability between the state-of-the-art in transparent array technologies and our ultra-high density transparent graphene array [5, 6, 8-27]. Extended Data Figure 1 plots optical transmittance as a function of normalized impedance for all the electrode technologies listed in Extended Data Table 1.

Supplementary Discussion 2

Although metal microwires offer low resistivity and could be miniaturized (Extended Data Fig. 2a,b) to achieve partial transparency for microelectrode arrays, they suffer from light-induced artifacts during two-photon imaging (Extended Data Fig. 2e,f). We conducted characterization experiments using 64-channel arrays with gold and graphene wires to further investigate these issues in gold arrays. Extended Data Figure 2d demonstrates the shadows formed by opaque gold wires at two different depths (50 and 250µm) during two-photon imaging, resulting in information loss by masking a subset of neurons. The signals recorded by gold and graphene electrodes (Extended Data Fig. 2d) during two-photon imaging (with a focal plane located 50µm below the electrode) show that significant light-induced artifacts are generated by the gold electrode, while no artifacts are present in the signals recorded by the graphene electrode. Extended Data Figure 2f illustrates the power spectral density of signals recorded by the graphene and gold electrodes during a two-photon Z-scan from 50µm to 150µm depth under the electrodes (with five frames at each level and 2µm steps). Unlike graphene, the signals recorded by the gold electrode contain all the harmonics of the two-photon scanning frequency (~30Hz), which would heavily distort neural recordings and make it quite impossible to interpret the electrical recordings in multimodal experiments. Therefore, microwires of the high-density arrays have to be made of

transparent materials to provide clear field of view across the entire recording area and eliminate the light-induced artifacts.

Supplementary Discussion 3

Our interlayer-doped double layer graphene (id-DLG) approach was effective in eliminating the defects formed in growth or fabrication of graphene. Figure 1c compares the graphene microwires made of single layer graphene (SLG) and id-DLG. SLG often exhibits defects that emerge during fabrication, which can lead to open circuits when the graphene is patterned to form microscale wires. These defects pose a constraint when trying to scale the graphene wires to build high-density and large area microelectrode arrays. These defects are randomly distributed over the graphene, and it is improbable to have overlapping defects across the top and bottom layers. Therefore, double layer graphene allows for continuous conductivity in extended microscale graphene wires, resulting in high yields (Fig. 1c and Extended Data Fig. 3). However, as the width of these long graphene wires is reduced, their resistance increases. HNO_3 is a well-known p-type dopant for graphene that induces a shift in the Fermi level by facilitating the transfer of surface charges between HNO_3 and carbon, which enhances the conductivity [28]. id-DLG formed with HNO_3 doping effectively reduces the graphene sheet resistance from 1908 Ω/sq (SLG) to 276 Ω/sq (id-DLG) (Fig. 1d), which enables us to shrink the graphene wires without any attenuation in recorded signals. It is important to note that double layer graphene (DLG) without interlayer dopants only reduces the sheet resistance to 606 Ω/sq (Fig. 1d).

Supplementary Discussion 4

Current peaks in CV measurements can provide information on electrochemical processes that occur at the interface (Extended Data Fig. 4d). The absence of redox peaks in the CV curve of id-DLG indicates that the electrolyte/id-DLG interface is fully capacitive. On the other hand, PtNP-deposited id-DLG shows surface oxide reduction peaks around -300 mV and hydrogen absorption peaks around -500 mV to -800 mV, showing that PtNPs are contributing to the charge transfer process at the electrode/electrolyte interface [11, 29]. Furthermore, the CV curves demonstrate a 7.5-fold increase in the charge storage capacity (CSC) following PtNP deposition, raising from 4.08 mC/cm^2 (id-DLG) to 30.72 mC/cm^2 (PtNP/id-DLG). This enhancement can be attributed to the large pseudo-capacitance of the PtNP interface and the increased surface roughness, which results in a larger effective surface area.

Supplementary Discussion 5

Although the length and resistance of graphene wires may vary across the array, their impact on the CV and EIS results is minimal. This is demonstrated in Extended Data Figure 4e, where the resistances of graphene wires prove to be substantially lower than the impedances of the electrodes (excluding the graphene wire resistances), regardless of the length of the graphene wires. Additionally, given the high input impedance of the amplifier (~10 MΩ), there is no substantial voltage drop on the graphene wires and attenuation in recorded signals. Hence, the length and resistance of the graphene wires have negligible effect on the electrode characterization results and electrophysiological recordings.

Supplementary Discussion 6

We specifically targeted the primary visual cortex (V1) as our focal region, given the diverse sensitivity to various visual stimuli attributes exhibited by V1 neural populations [30-32]. Notably, V1 neurons demonstrate a wide range of direction and orientation selectivity when stimulated by drifting gratings [33-35]. Consequently, the extensive and heterogeneous datasets obtained from these experiments serves as valuable resources for conducting various types of multimodal data analyses.

Supplementary Discussion 7

To investigate the impact of population coupling on single-cell calcium activity inference, we computed the population couplings for the 114 common cells in the evoked and spontaneous sessions. To calculate the population coupling (c_i) for the L2/3 neurons in the spontaneous and evoked sessions, we employed the following equations from the literature [36, 37]:

$$c_i = \frac{1}{\|f_i\|} \int f_i(t) \sum_{j \neq i} \left(f_j(t) - \mu_j\right) dt \quad (1)$$

$$c_i = corr(f_i, \frac{1}{N-1} \sum_{j \neq i}^{N} f_j) \quad (2)$$

In these equations, $f_i(t)$ is the calcium fluorescence change (ΔF/F) of individual cell i at timepoint t, μ_j is the average ΔF/F of cell j over time, $\|f_i\|$ is the standard deviation of ΔF/F for cell i over time, and N is the number of cells.

We found that the population couplings are quite diverse in both sessions (spontaneous and evoked) and several neurons have calcium activities that are invariant to the stimuli and have similar levels of population coupling in the evoked and spontaneous recordings (Extended Data

Fig. 8a,b). We also found that some of the neurons are highly coupled to the population activity in the spontaneous sessions but not in the evoked sessions and vice versa (highlighted with blue and red dots in Extended Data Fig. c,d). These findings suggest a complex and heterogenous relationship between V1 population activity and visual stimuli. Our examination of the decoding results in relation to population coupling revealed an unintuitive relationship between decoding performance and population coupling (Extended Data Fig. 8c,d). For example, we found highly coupled cells that exhibited poor decoding results (highlighted with green boxes in Extended Data Fig. 8c,d). On the other hand, some of the top decoded cells showed low levels of population coupling (highlighted with yellow boxes in Extended Data Fig. 8c,d). To investigate whether top decoded cells tend to have high population coupling, as one might expect that population coupled activity drives the bulk of cortical surface potential modulation, we focused on cells with high decoding performance. We calculated the population coupling for different numbers of top decoded cells and compared them with decoding results. We found that the decoding accuracy for the top inferred cells was consistently better in the evoked sessions, despite having lower population coupling compared to the spontaneous sessions (Extended Data Fig. 8e-h).

Supplementary Figures

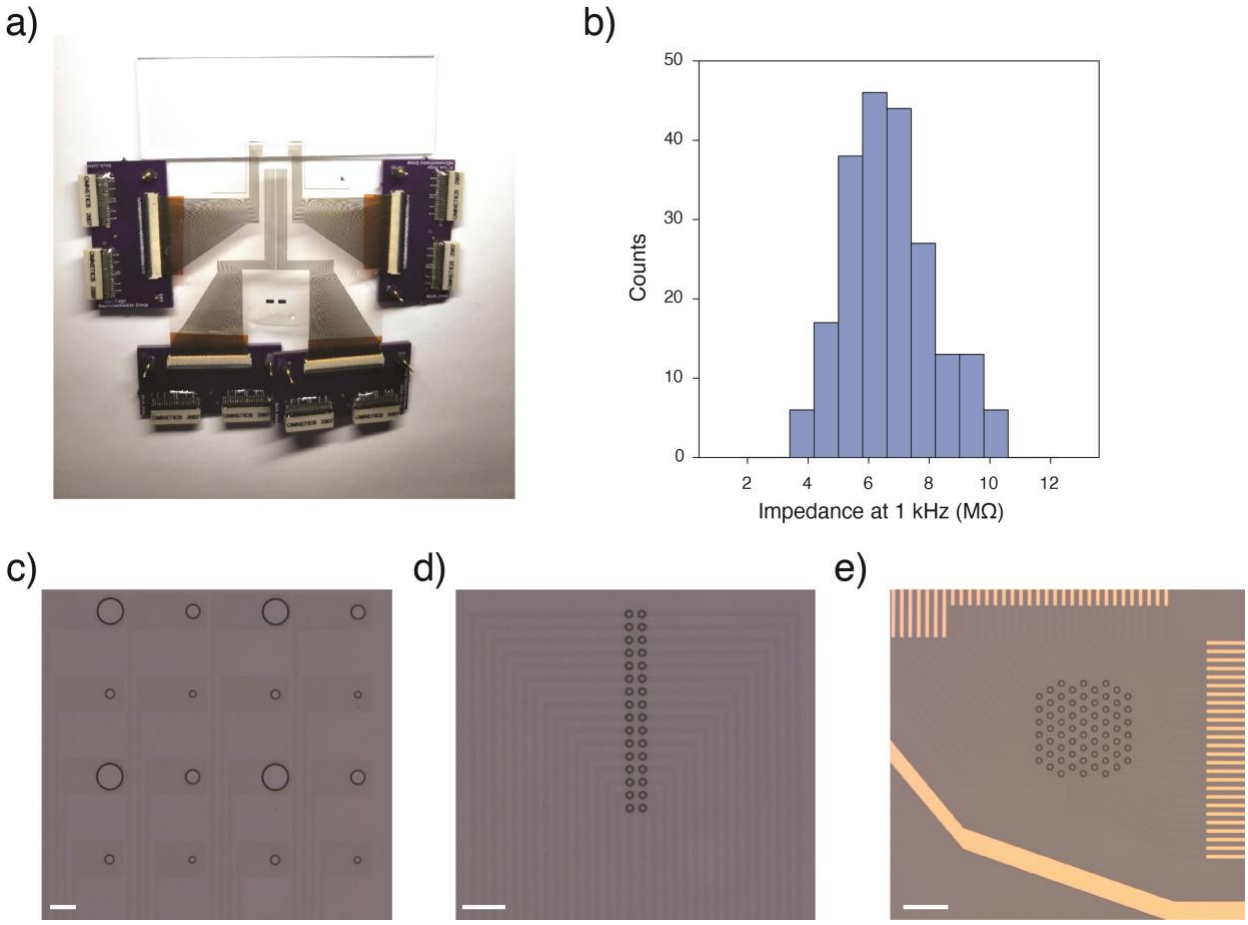

Supplementary Fig. 1. Various design of fabricated graphene arrays. (a) 256-channel transparent graphene array connected to the recording interface boards. (b) Histogram of the impedance of 256-channel graphene array. (c) Microscopy image of graphene array with various opening sizes (20 μm, 30 μm, 50 μm, and 100 μm in diameter) and center-to-center pitch of 350 μm. (d) Microscopy image of 32-channel graphene array with center-to-center pitch of 30 μm. (e) Microscopy image of ultra-dense 64-channel graphene array with center-to-center pitch of 50 μm. Scale bars are 100 μm.

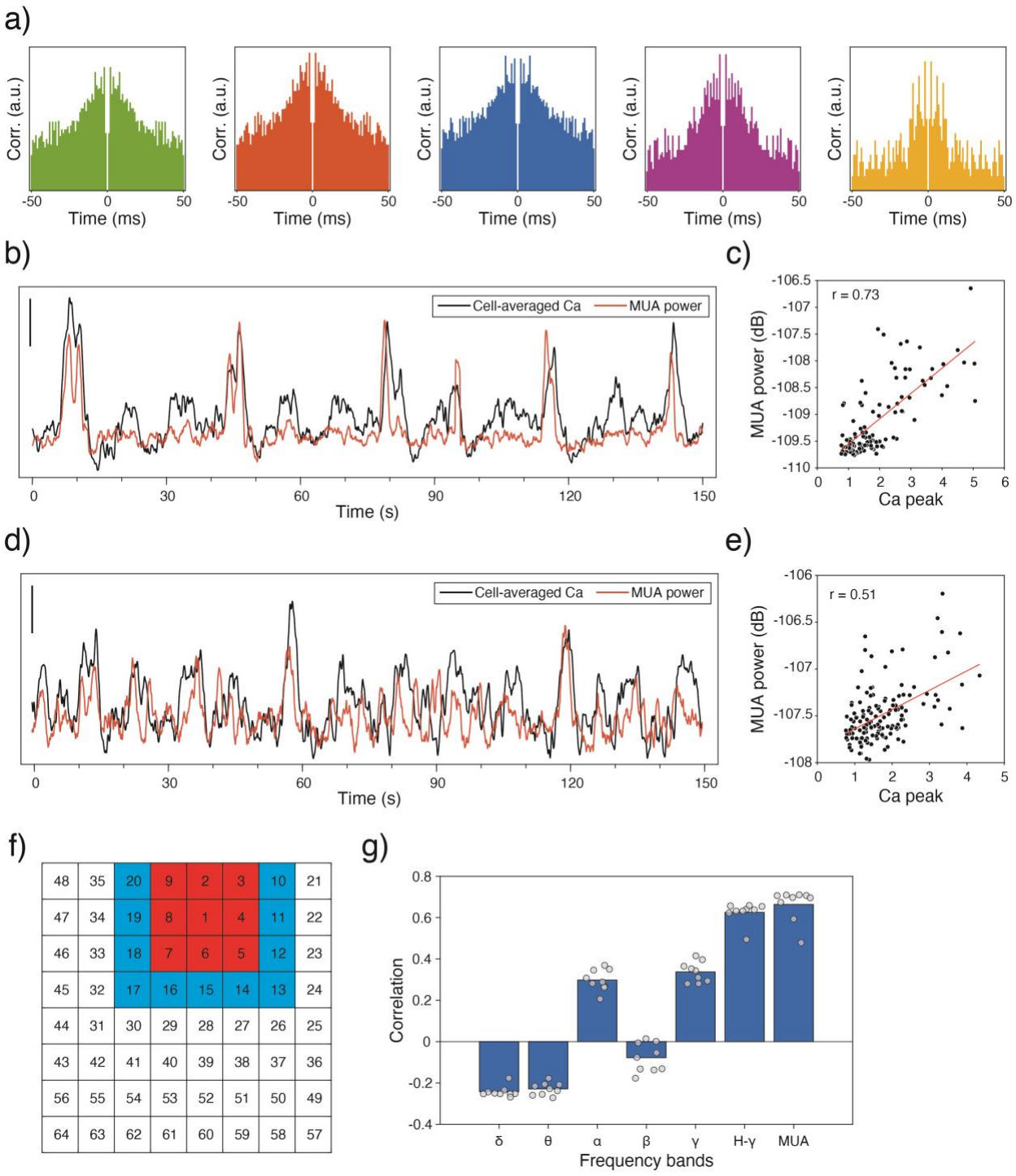

Supplementary Fig. 2. MUA and its correlation with calcium activity. (a) Representative autocorrelograms of detected units show no refractory periods which suggests that these units are MUAs. (b-e) Correspondence between cell-averaged calcium signals and MUA power from two other experiments with 16-channel arrays. (b) Representative cell-averaged ΔF/F and MUA power of the channel with maximum correlation and (c) scatter plot of calcium peaks and MUA

powers for the channel with maximum correlation for mouse 2. (d,e) Same as b and c for mouse 3. The scale bar in b is 2 z-score for calcium and 1 dB for MUA power. The scale bar in d is 2 z-score for calcium and 0.5 dB for MUA power. (f) The order of channels used for decoding calcium signals. The red area shows the imaging FoV, and the blue area indicates the closest 11 channels around the FoV. (g) The correlation between cell-averaged calcium peaks and surface potential powers around the peak onsets at different frequency bands for the 9 channels in the FoV (red area in f). The gray dots show the correlation values for the 9 channels and the blue bars show the average correlation values of 9 channels in the FoV.

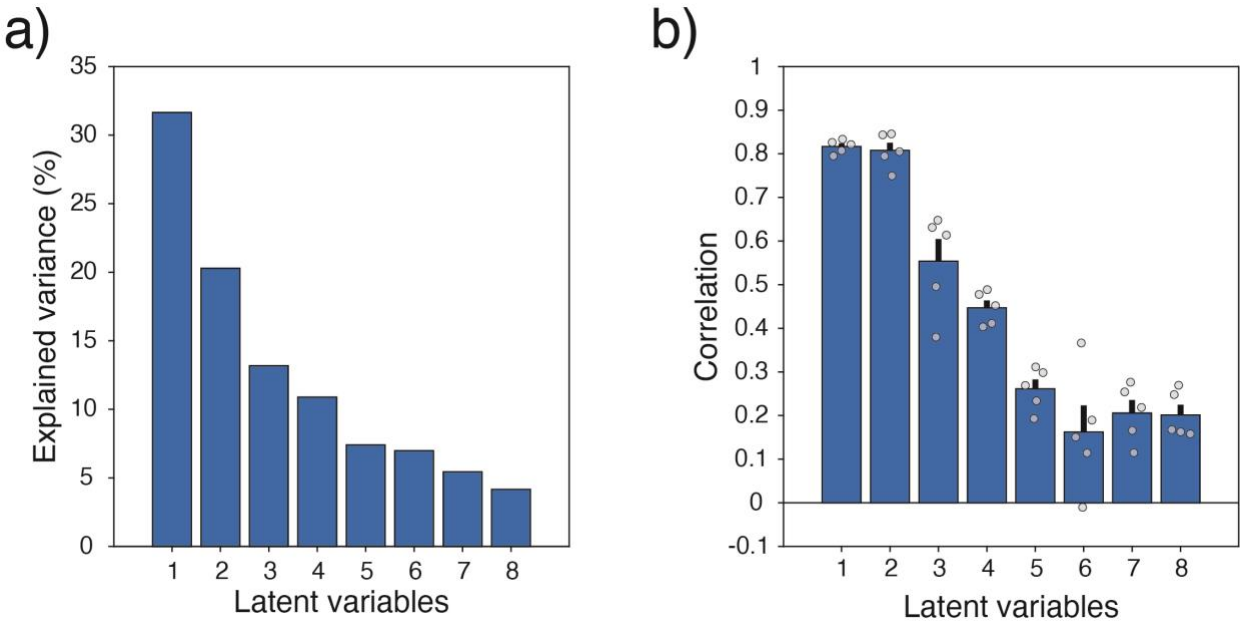

Supplementary Fig. 3. Low dimensional latent space. (a) Explained variance of the high dimensional calcium signal by each latent variable. (b) Decoding results of the eight latent variables averaged over five folds. The blue bars and black lines indicate the mean and s.e.m., respectively (n=5). The gray circles show individual folds.

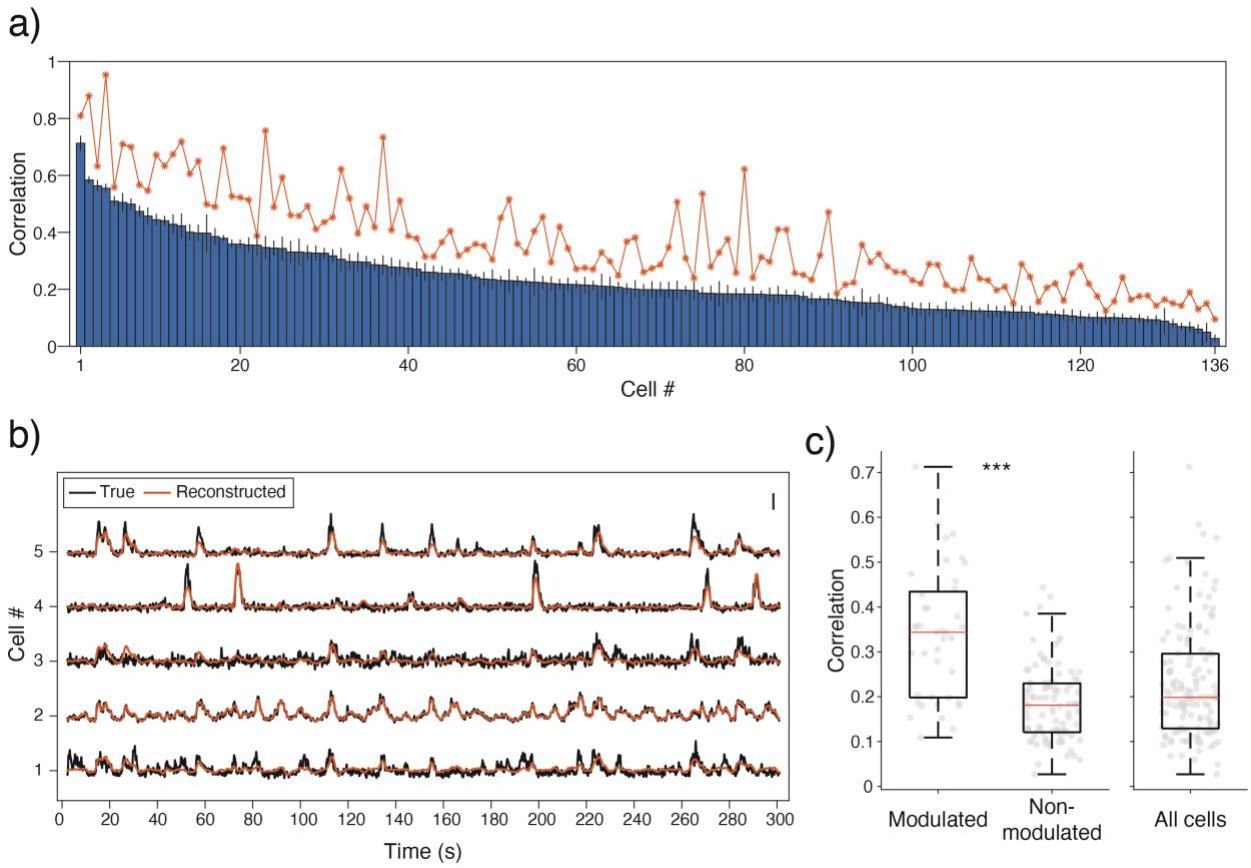

Supplementary Fig. 4. Decoding calcium signals at single-cell resolution. (a) The blue bars show decoding results (averaged over 5 folds) for all 136 cells using the inferred (predicted) latent variables. The black lines indicate the s.e.m. The orange line shows the maximum correlation that could be achieved when true latent variables are used for reconstructing single-cell activities. (b) Representative examples for reconstructed single-cell activities (same cells shown in Fig. 6b) using true latent variables (orange) vs ground truth ΔF/F (black). The scale bar is 3 z-score. (c) Decoding results for the modulated (n=40) vs non-modulated cells (n=96). The box plots are defined in terms of center (median), bounds of box (interquartile range (IQR) 25th and 75th percentile), whiskers (minimum and maximum within 1.5 IQR). Two-sided Wilcoxon rank sum test ($p<0.001$).

References

1. Lim, K., et al., *Flexible PEDOT: PSS/ITO hybrid transparent conducting electrode for organic photovoltaics.* Solar energy materials and solar cells, 2013. **115**: p. 71-78.
2. Tran, D.-P., H.-I. Lu, and C.-K. Lin, *Conductive characteristics of indium tin oxide thin film on polymeric substrate under long-term static deformation.* Coatings, 2018. **8**(6): p. 212.
3. Hansen, S.F. and A. Lennquist, *Carbon nanotubes added to the SIN List as a nanomaterial of Very High Concern.* Nature Nanotechnology, 2020. **15**(1): p. 3-4.
4. Sakamoto, Y., et al., *Comparative study for carcinogenicity of 7 different multi-wall carbon nanotubes with different physicochemical characteristics by a single intraperitoneal injection in male Fischer 344 rats.* The Journal of toxicological sciences, 2018. **43**(10): p. 587-600.
5. Neto, J.P., et al., *Transparent and flexible electrocorticography electrode arrays based on silver nanowire networks for neural recordings.* ACS Applied Nano Materials, 2021. **4**(6): p. 5737-5747.
6. Qiang, Y., et al., *Transparent arrays of bilayer-nanomesh microelectrodes for simultaneous electrophysiology and two-photon imaging in the brain.* Science advances, 2018. **4**(9): p. eaat0626.
7. Cui, X.T. and D.D. Zhou, *Poly (3, 4-ethylenedioxythiophene) for chronic neural stimulation.* IEEE Transactions on Neural Systems and Rehabilitation Engineering, 2007. **15**(4): p. 502-508.
8. Kuzum, D., et al., *Transparent and flexible low noise graphene electrodes for simultaneous electrophysiology and neuroimaging.* Nature communications, 2014. **5**(1): p. 5259.
9. Park, D.-W., et al., *Graphene-based carbon-layered electrode array technology for neural imaging and optogenetic applications.* Nature communications, 2014. **5**(1): p. 5258.
10. Park, D.-W., et al., *Electrical neural stimulation and simultaneous in vivo monitoring with transparent graphene electrode arrays implanted in GCaMP6f mice.* ACS nano, 2018. **12**(1): p. 148-157.
11. Lu, Y., et al., *Ultralow impedance graphene microelectrodes with high optical transparency for simultaneous deep two-photon imaging in transgenic mice.* Advanced functional materials, 2018. **28**(31): p. 1800002.
12. Thunemann, M., et al., *Deep 2-photon imaging and artifact-free optogenetics through transparent graphene microelectrode arrays.* Nature communications, 2018. **9**(1): p. 2035.
13. Liu, X., et al. *Decoding ECoG High Gamma Power from Cellular Calcium Response using Transparent Graphene Microelectrodes*. in *2019 9th International IEEE/EMBS Conference on Neural Engineering (NER)*. 2019. IEEE.
14. Driscoll, N., et al., *Multimodal in vivo recording using transparent graphene microelectrodes illuminates spatiotemporal seizure dynamics at the microscale.* Communications biology, 2021. **4**(1): p. 1-14.

15. Wilson, M.N., et al., *Multimodal monitoring of human cortical organoids implanted in mice reveal functional connection with visual cortex.* Nature Communications, 2022. **13**(1): p. 7945.
16. Liu, X., et al., *E-Cannula reveals anatomical diversity in sharp-wave ripples as a driver for the recruitment of distinct hippocampal assemblies.* Cell Reports, 2022. **41**(1): p. 111453.
17. Ledochowitsch, P., et al. *A transparent μECoG array for simultaneous recording and optogenetic stimulation*. in *2011 Annual International Conference of the IEEE Engineering in Medicine and Biology Society*. 2011. IEEE.
18. Kwon, K.Y., et al., *Opto-μECoG array: A hybrid neural interface with transparent μECoG electrode array and integrated LEDs for optogenetics.* IEEE transactions on biomedical circuits and systems, 2013. **7**(5): p. 593-600.
19. Kunori, N. and I. Takashima, *A transparent epidural electrode array for use in conjunction with optical imaging.* Journal of neuroscience methods, 2015. **251**: p. 130-137.
20. Zhang, J., et al., *Stretchable transparent electrode arrays for simultaneous electrical and optical interrogation of neural circuits in vivo.* Nano letters, 2018. **18**(5): p. 2903-2911.
21. Toda, H., et al., *Simultaneous recording of ECoG and intracortical neuronal activity using a flexible multichannel electrode-mesh in visual cortex.* Neuroimage, 2011. **54**(1): p. 203-212.
22. Seo, J.W., et al., *Artifact-free 2D mapping of neural activity in vivo through transparent gold nanonetwork array.* Advanced Functional Materials, 2020. **30**(34): p. 2000896.
23. Araki, T., et al., *Long-term implantable, flexible, and transparent neural interface based on Ag/Au core–shell nanowires.* Advanced Healthcare Materials, 2019. **8**(10): p. 1900130.
24. Chen, Z., et al., *Flexible and transparent metal nanowire microelectrode arrays and interconnects for electrophysiology, optogenetics, and optical mapping.* Advanced Materials Technologies, 2021. **6**(7): p. 2100225.
25. Kshirsagar, P., et al., *Transparent Graphene/PEDOT: PSS microelectrodes for electro-and optophysiology.* Advanced Materials Technologies, 2019. **4**(1): p. 1800318.
26. Yang, W., et al., *A fully transparent, flexible PEDOT: PSS–ITO–Ag–ITO based microelectrode array for ECoG recording.* Lab on a Chip, 2021. **21**(6): p. 1096-1108.
27. Cho, Y.U., et al., *Ultra-low cost, facile fabrication of transparent neural electrode array for electrocorticography with photoelectric artifact-free optogenetics.* Advanced Functional Materials, 2022. **32**(10): p. 2105568.
28. Das, S., et al., *Effect of HNO 3 functionalization on large scale graphene for enhanced tri-iodide reduction in dye-sensitized solar cells.* Journal of Materials Chemistry, 2012. **22**(38): p. 20490-20497.
29. Liu, X., et al., *Multimodal neural recordings with Neuro-FITM uncover diverse patterns of cortical–hippocampal interactions.* Nature neuroscience, 2021. **24**(6): p. 886-896.

30. Hubel, D.H. and T.N. Wiesel, *Receptive fields, binocular interaction and functional architecture in the cat's visual cortex.* The Journal of physiology, 1962. **160**(1): p. 106.
31. Hubel, D.H. and T.N. Wiesel, *Receptive fields and functional architecture of monkey striate cortex.* The Journal of physiology, 1968. **195**(1): p. 215-243.
32. Kohn, A. and M.A. Smith, *Stimulus dependence of neuronal correlation in primary visual cortex of the macaque.* Journal of Neuroscience, 2005. **25**(14): p. 3661-3673.
33. Ohki, K., et al., *Functional imaging with cellular resolution reveals precise micro-architecture in visual cortex.* Nature, 2005. **433**(7026): p. 597-603.
34. Zhang, Y., et al., *Fast and sensitive GCaMP calcium indicators for imaging neural populations.* Nature, 2023. **615**(7954): p. 884-891.
35. Tang, M.F., et al., *Expectation violations enhance neuronal encoding of sensory information in mouse primary visual cortex.* Nature Communications, 2023. **14**(1): p. 1196.
36. Okun, M., et al., *Diverse coupling of neurons to populations in sensory cortex.* Nature, 2015. **521**(7553): p. 511-515.
37. Sweeney, Y. and C. Clopath, *Population coupling predicts the plasticity of stimulus responses in cortical circuits.* Elife, 2020. **9**: p. e56053.